THE ASTROPHYSICAL JOURNAL, Vol 154, October 1968

# A THEORY OF DUST COMETS. II. RESULTS FOR COMET AREND-ROLAND

MICHAEL L. FINSON AND RONALD F. PROBSTEIN
Department of Mechanical Engineering, Massachusetts Institute of Technology

*Received November 24, 1967*

## ABSTRACT

Surface densities in the tail of Comet Arend-Roland 1956h are calculated using the theory of Paper I. The distributions of surface density are compared with measured distributions of light intensity from which the dust and head-gas emission rates as functions of time, the distribution of dust-particle sizes, and the emission velocity from the inner head region as a function of particle size and time are determined essentially for the first time Dust-particle diameters on the order of 1 $\mu$ are found, consistent with previous estimates. The deduced particle-size distribution is qualitatively similar to those found for the interplanetary dust particles from studies of the zodiacal light and to one suggested from an analysis of the continuous spectra from the heads of Comets Arend-Roland and Mrkos. For Comet Arend-Roland, near its perihelion, dust emission rates $\sim$7 5 $\times$ $10^7$ g sec$^{-1}$ and gas emission rates $\sim$1 5 $\times$ $10^{30}$ molecules sec$^{-1}$ are found, confirming previous estimates An outburst in the dust emission is deduced to have occurred in Comet Arend-Roland on April 2, 1957, about 6 days before perihelion, and the "forward spike" of this comet is found to consist of particles emitted between February 6 and March 1, 1957.

As a general property of dust-rich comets, it is suggested that they emit larger amounts of dust during their approach to the Sun than during recession.

## I. INTRODUCTION

In the first part of this work (Finson and Probstein 1968; hereinafter referred to as "Paper I") equations were presented for the calculation of modified distributions of surface density in the tails of dust comets. These results were derived from a model in which dust particles having a wide distribution of sizes are released from the comet nucleus in an essentially continuous manner in time during the period of distinctive cometary phenomena as a result of solar heating. The dust particles were taken to be accelerated radially outward from the nucleus by drag forces due to the expanding head gas. This interaction was found to take place only in a small inner head region where the gas may be described as a continuum. In the tail region the only significant forces which were assumed to act on the dust particles were solar gravity and pressure of solar radiation. The motion of the dust particles in the tail was treated as a "hypersonic," collision-free flow in a smaller "effective" gravity field.

The expressions obtained for the surface density (modified so as to be proportional to the light intensity) involved three unknown functional parameters: $\dot{N}_d(t)$, $f(1-\mu)$, and $v_i(1-\mu, \tau; t_c)$. The first two functions are, respectively, the emission rate of the dust from the comet nucleus and a distribution function which can be related to the particle-size distribution. The third function is the initial velocity of the dust particles corresponding to the terminal velocity which the dust particles reach in the neighborhood of the nucleus as a result of being accelerated outward from the nucleus by the expanding head gas. One of the two independent variables is the time of emission $t$, which is taken to be zero at perihelion. Here $t = t_c - \tau$, where $t_c$ is the time of observation (considered to be fixed and thus a known parameter of the problem), with emission occurring $\tau$ units of time earlier. The other independent variable is $1-\mu$, defined as the ratio of the force due to radiation to that of gravity acting on a dust particle. It was shown in Paper I that we may write

$$1 - \mu = C(\rho_d d)^{-1}\,, \qquad (1)$$

© American Astronomical Society • Provided by the NASA Astrophysics Data System

1968ApJ...154..353F

where $C = 1.19 \times 10^{-4}\, Q_{\rm pr}$ g cm$^{-2}$, with $Q_{\rm pr}$ the scattering efficiency for radiation pressure, taken constant for all particle sizes, and $d$ the diameter of a spherical particle of mass density $\rho_d$.

We shall now discuss the manner in which the equations derived in Paper I may be used to calculate density distributions for the comet dust tail. The specific case of Comet Arend-Roland 1956h will be considered, and calculations performed for that comet will be compared with measured distributions of light intensity. In the calculation we shall assume that the three parametric functions involved are given or have been selected, rather than the reverse procedure of the determination of these functions from given (i.e., measured) density distributions. While the latter process is of greater interest, the results given in Paper I cannot conveniently be expressed in such a form as to allow this to be done directly. Therefore, we shall first present calculated density distributions for Comet Arend-Roland based on assumed functional forms for $f(1 - \mu)$, $\dot{N}_d(t)$, and $v_i(1 - \mu, t)$, which have been selected for optimal agreement between the calculated and measured distributions. In what follows we will then discuss the manner of selection of these functions and their uniqueness.

TABLE 1

ORBIT CHARACTERISTICS FOR COMET AREND-ROLAND

| Date (1957 U T.) | $t_c \times 10^{-6}$ (sec) | $r_c$ (a u.) | $\Delta$ (a u ) |
|---|---|---|---|
| April 27 8 | 1 71 | 0 64 | 0 66 |
| April 29 9 | 1 89 | 68 | 71 |
| May 1 9 | 2 06 | .72 | .76 |
| May 2 9 | 2.15 | 0 74 | 0 79 |

## II. TAIL SURFACE DENSITY AND COMPARISON WITH OBSERVATIONS

Table 1 gives the dates of principal interest in the calculations of density distributions for Comet Arend-Roland, along with the times of observation $t_c$, the Sun-comet distances $r_c$, and the Earth-comet distances $\Delta$. For this comet, perihelion occurred on April 8, 1957, when $t \equiv 0$, and the perihelion distance was 0.316 a.u. Most of the detailed observations of this comet were made during the period represented by the dates given in Table 1, when the comet was most favorably situated for observation. Figure 1, *a–d*, shows syndyne ($1 - \mu =$ const.) and synchrone ($\tau =$ const.) loci for Comet Arend-Roland for the four dates listed in Table 1, as projected onto the photographic plane. The photographic plane is defined as that plane which contains the comet nucleus and is normal to the line joining the nucleus and the Earth. The syndyne and synchrone loci in this plane may be expressed by the functional relations

$$M_{\rm CM} = M_{\rm CM}(1 - \mu, \tau; t_c)\ , \quad N_{\rm CM} = N_{\rm CM}(1 - \mu, \tau; t_c)\ . \tag{2}$$

We recall that the $M$ coordinate is the apparent radial direction with the $N$ coordinate perpendicular to $M$ and directed opposite to the comet's motion along its orbit. The calculation of these syndynes and synchrones has been carried out as described in Appendices A and B of Paper I. The extent of these curves and the ranges of $1 - \mu$ and $\tau$ shown are roughly consistent with the extent of the observed dust tail of the comet. Exceptions are the synchrones for very high $\tau$'s or very early emissions, which have been included for the first two dates for later use in connection with the observed "forward spike" of this comet. The change in behavior with time of the synchrones and syndynes is due partly to the actual development of the tail with progressing time and partly to the changing position of the Earth with respect to the comet.

© American Astronomical Society • Provided by the NASA Astrophysics Data System

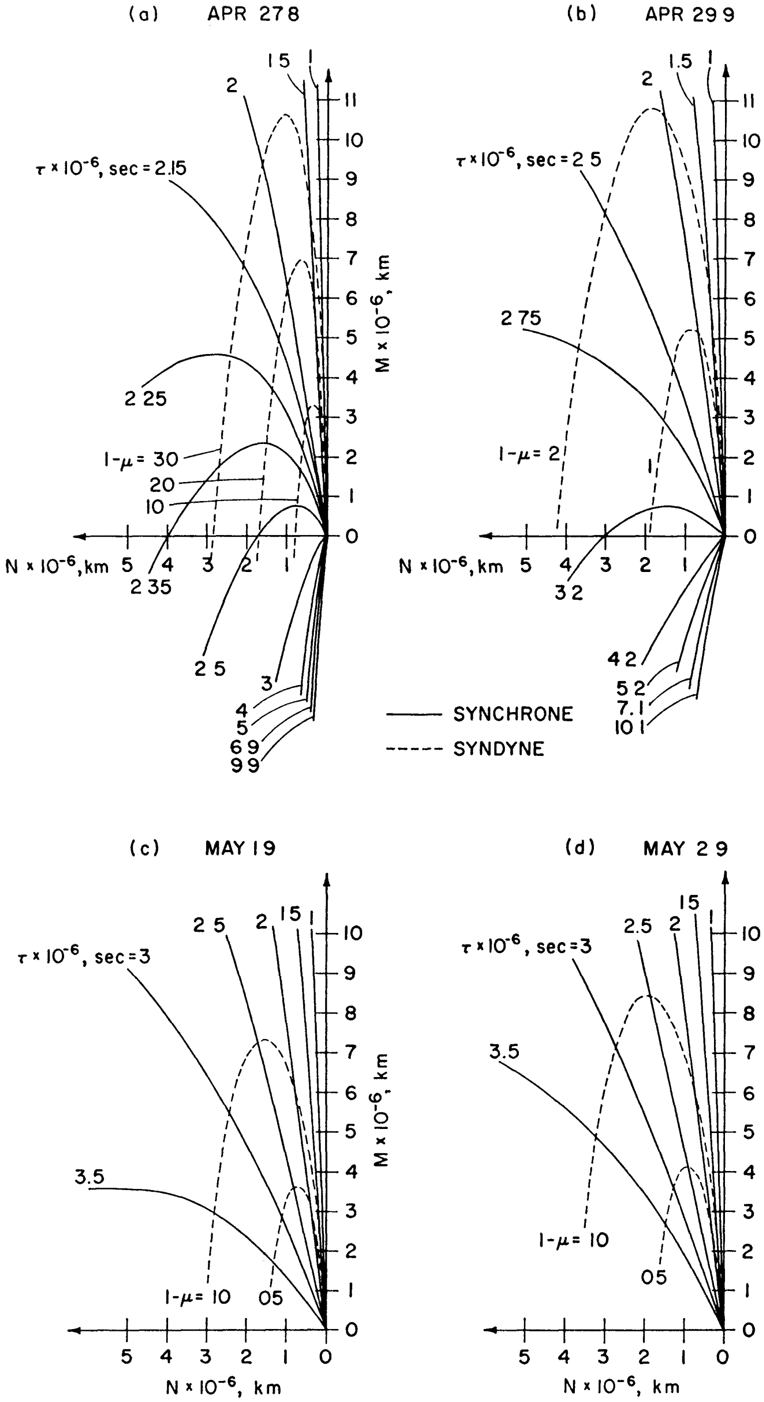

FIG. 1.—Syndyne and synchrone loci in photographic plane for Comet Arend-Roland

In Figure 1 it is apparent that the synchrones have a much less complicated shape than do the syndynes. The synchrones "fan out" from the nucleus at increasing angles to the radial direction (the $M$-axis) with increasing values of $\tau$, and, except for the larger $\tau$ values shown on the first two dates, these loci are nearly straight lines, with the distance from the nucleus along a given synchrone nearly proportional to $1 - \mu$. Accordingly, for, say, $\tau < 2 \times 10^6$ sec on April 27.8, for $\tau < 3 \times 10^6$ sec on April 29.9, and for all the $\tau$'s shown on the later two dates, the synchrone curves can be well represented by expressions of the form

$$\begin{aligned} M_{\mathrm{CM}}(1 - \mu; \tau, t_c) &= c_1(\tau, t_c) \cdot (1 - \mu) + c_2(\tau, t_c) \cdot (1 - \mu)^2 \,, \\ N_{\mathrm{CM}}(1 - \mu; \tau, t_c) &= c_3(\tau, t_c) \cdot (1 - \mu) + c_4(\tau, t_c) \cdot (1 - \mu)^2 \,, \end{aligned} \tag{3}$$

in which the quadratic terms are generally small. For each synchrone $c_1 - c_4$ can be determined from an exact calculation at two different values of $1 - \mu$. A similar expression for this comet, and probably for other comets, could be applied to synchrone loci in the comet orbit plane.

In contrast to the synchrones, the syndynes attain a maximum value of $M$, which occurs at a value of $\tau$ corresponding to the perihelion passage or somewhat earlier. These curves cannot be represented by, or approximated by, a simple function of $\tau$ over the ranges of $\tau$'s shown. Taylor-series expansions were originally derived by Bredichin for the syndyne loci in the comet orbit plane (see, e.g., Wurm 1963). However, such expressions, being expansions in $\tau$ about $\tau = 0$, are useful principally in the inner tail and head regions, for much smaller values of $\tau$ than those considered here. It should be noted that the strong curvature of the syndyne curves is not unique to the comet being considered, although the effect is accentuated in the case of Comet Arend-Roland because of the proximity of the Earth to the comet orbit plane.

Two approaches were used in Paper I in deriving the modified surface density. In one the tail density was found by integrating over different synchrone tails, each of which is made up of particles emitted at one time; in the other the density was obtained by integrating over different syndyne tails, each of which is made up of particles of one size. In carrying out the integrations, a "hypersonic" approximation was introduced. This approximation was satisfied in the synchrone approach if

$$\frac{dx}{d(1 - \mu)} = \left\{ \left[ \frac{\partial M_{\mathrm{CM}}}{\partial(1 - \mu)} \right]^2 + \left[ \frac{\partial N_{\mathrm{CM}}}{\partial(1 - \mu)} \right]^2 \right\}^{1/2} \gg \frac{v_i \tau}{1 - \mu} \tag{4a}$$

and in the syndyne approach if

$$\frac{dx}{d\tau} = \left[ \left( \frac{\partial M_{\mathrm{CM}}}{\partial \tau} \right)^2 + \left( \frac{\partial N_{\mathrm{CM}}}{\partial \tau} \right)^2 \right]^{1/2} \gg v_i \,. \tag{4b}$$

Let us now evaluate the validity of the hypersonic approximations. For the synchrone case equations (3) permit the derivatives in equation (4a) to be simply approximated. Neglecting the quadratic terms in equations (3) and taking into account the fact that most synchrones make a small angle with the $M$-axis, we have at a given value of $M$

$$\frac{dx}{d(1 - \mu)} \approx \frac{M}{1 - \mu} \,, \tag{5}$$

so that inequality (4a) may be rewritten as

$$\frac{v_i \tau}{M} \ll 1 \,. \tag{6}$$

1968ApJ...154..353F

The quantity $v_i\tau/M$ is the relative width of a synchrone tail. Table 2 presents values of this quantity for the first and last dates of observation mentioned above, for values of $M$ and $\tau$ encompassing the range of interest. Typically $v_i$ is about 0.3 km sec$^{-1}$ or less, although the actual values of $v_i$ given by the function $v_i(1 - \mu, \tau; t_c)$, to be discussed below, were used for the estimates made. For $\tau = 2.25 \times 10^6$ sec on April 27.8, when the approximation of equations (3) becomes poor, the more accurate values taken directly from the orbit-mechanical calculations were used. From Paper I, the relative error incurred in the hypersonic approximation is of the order of $(v_i\tau/M)^2$, so that from Table 2 the synchrone approach is seen to be accurate to within 10 per cent, except for $M < 10^6$ km, and for $\tau > 2 \times 10^6$ sec on April 27.8.

The hypersonic approximation given by equation (4b) for the syndyne approach is not as well satisfied. The "velocity" of the motion along an individual syndyne, $dx/d\tau$, varies considerably with $\tau$, in contrast to the near-constancy of $dx/d(1 - \mu)$ along a synchrone. Starting from a value of zero at the nucleus, $dx/d\tau$ increases with increasing $\tau$ along the "ascending" portion of a given syndyne. However, near the maximum of the curves, $dx/d\tau$ decreases to a local minimum and increases considerably with further increase in $\tau$ on the "descending" portion of the loci. The low value of $dx/d\tau$ for small $\tau$ precludes a hypersonic approximation within, say, $10^6$ km of the nucleus, as was also the case with the synchrones. Near the relative maxima of the syndyne curves, the hypersonic condition is also not well satisfied.

TABLE 2

VALUES OF $v_i\tau/M$ FOR COMET AREND-ROLAND

APRIL 27 8

| $M \times 10^{-6}$ (km) | $\tau = 10^6$ sec | $\tau = 2 \times 10^6$ sec | $\tau = 2\ 25 \times 10^6$ sec |
|---|---|---|---|
| 1 | 0 20 | 0 40 | 0 45 |
| 2 | 115 | 25 | 31 |
| 4 | 0 066 | 0 16 | 0 23 |

MAY 2 9

| $M \times 10^{-6}$ (km) | $\tau = 10^6$ sec | $\tau = 2 \times 10^6$ sec | $\tau = 2\ 6 \times 10^6$ sec | $\tau = 3 \times 10^6$ sec |
|---|---|---|---|---|
| 1 | 0 25 | 0 27 | 0 26 | 0 17 |
| 3 | 10 | 16 | 17 | 11 |
| 8 | 0 05 | 0 08 | 0 09 | 0 06 |

Table 3 gives the minimum value of $dx/d\tau$ at the relative maxima of the various syndyne curves on April 27.8 and May 2.9, as well as the quantity $v_i/(dx/d\tau)_{\min}$. The values of $(dx/d\tau)_{\min}$ given were obtained directly from the orbit-mechanical calculations. From Table 3 it is evident that, in the vicinity of the maxima of the syndyne curves, the hypersonic condition of equation (4b) is not well satisfied. However, for values of $\tau \geq 2 \times 10^6$ sec on April 27.8, where we have seen that the synchrone curves tend to degenerate and become less hypersonic, the hypersonic syndyne approach becomes valid. In this range we are concerned with positions on the syndynes well past the maxima. For a typical value such as $1 - \mu = 0.10$ and $\tau = 2.3 \times 10^6$ sec on April 27.8, $dx/d\tau \approx 5.4$ km sec$^{-1}$, so that $v_i/(dx/d\tau) \approx 0.05$. Thus the only region of interest where the hypersonic synchrone approach might not be valid or convenient is well handled by the hypersonic syndyne approach. The calculations for Comet Arend-Roland to be presented employed

© American Astronomical Society • Provided by the NASA Astrophysics Data System

1968ApJ...154..353F

the synchrone approach entirely for April 29.9, May 1.9, and May 2.9 and for $\tau < 2 \times 10^6$ sec on April 27.8. For $\tau > 2 \times 10^6$ sec on the latter date the syndyne approach was used, since the synchrone hypersonic condition was not well satisfied and the curved shape of the synchrone axes made the calculations inconvenient. Here the complete range of $\tau$ integration was split into two ranges, with the individual integrals handled differently.

It should be noted that because of the projection effects connected with Arend-Roland, this comet probably represents a rather severe case in comparison with other comets with respect to the satisfaction of the hypersonic approximations. This follows from the fact that the actual tail length is some 4–5 times the apparent tail length. For more typical projection effects, where the appearance in the photographic plane would be similar to that in the orbit plane, the values of $dx/d\tau$ and $dx/d(1-\mu)$ would be 4–5 times those quoted above, and the respective hypersonic conditions would be that much more easily met.

TABLE 3

VALUES OF $(dx/d\tau)_{\min}$ AND $v_i/(dx/d\tau)_{\min}$ FOR COMET AREND-ROLAND

| $1-\mu$ | $M_{\max}\times 10^{-6}$ (km) | $(dx/d\tau)_{\min}$ (km sec$^{-1}$) | $v_i/(dx/d\tau)_{\min}$ |
|---|---|---|---|
| | April 27.8 ($\tau_{\max} \approx 1.8 \times 10^6$ sec) | | |
| 0.025 | 0.86 | 0.15 | 1.33 |
| .050 | 1.7 | 0.30 | 0.83 |
| .100 | 3.5 | 0.65 | 0.39 |
| .150 | 5.2 | 1.03 | 0.25 |
| | May 2.9 ($\tau_{\max} \approx 2.5 \times 10^6$ sec) | | |
| .0250 | 2.1 | 0.43 | 0.47 |
| .0375 | 3.1 | 0.68 | .33 |
| .0500 | 4.2 | 0.95 | .25 |
| 0.0750 | 6.2 | 1.50 | 0.17 |

We now turn to the integrations necessary to determine the modified surface density at a given point. With the synchrone approach, the density at a given point of interest $M_0,N_0$ was shown in Paper I to be given by

$$D = \int_{\tau_a}^{\tau_b} N_d f(1-\mu)\left[2v_i\tau \frac{dx}{d(1-\mu)}(1-\mu;\tau,t_c)\right]^{-1} d\tau\,. \tag{7}$$

Here the integrand represents the surface density for a differential synchrone tail. The synchrone locus for the particular value of $\tau$ serves as the axis of such a differential tail. The surface density is constant along a normal to this axis for distances less than $v_i\tau$ from the axis and is zero for distances greater than $v_i\tau$ from the axis. In evaluating this integral, one must simultaneously solve the equation for the normal containing the point $M_0,N_0$:

$$-\frac{\partial N_{\rm CM}/\partial(1-\mu)}{\partial M_{\rm CM}/\partial(1-\mu)} = \frac{M_0 - M_{\rm CM}}{N_0 - N_{\rm CM}}\,, \tag{8}$$

© American Astronomical Society • Provided by the NASA Astrophysics Data System

to obtain $1-\mu$ as a function of $M_0,N_0$ and $\tau$, with the functions $M_{\mathrm{CM}},N_{\mathrm{CM}}$ given by the appropriate orbit mechanics. The limits on the integral are the limiting values of $\tau$ for which the point of interest lies within the individual synchrone tails.

The most straightforward, and probably the most efficient, method of integrating equation (7) is simply to add together the contributions for a large number of $\tau$'s. This amounts to a superposition of a large number of differential synchrone tails. To do this, we may enumerate five distinct steps in the process:

1. First, the orbit mechanics must be used to determine $M_{\mathrm{CM}},N_{\mathrm{CM}}$ for a particular $\tau$ value and for all values of $1-\mu$. For Comet Arend-Roland it is possible to express the results of these calculations in the approximate, analytic form of equations (3).

2. For each grid point of interest, $M_0,N_0$, the value of $1-\mu$ for the normal line containing the point $M_0,N_0$ must be found by solving equation (8). Combining equations (3) with equation (8) produces a cubic equation in $1-\mu$ which can be solved analytically but is more efficiently solved by numerical iteration. When it is not possible to use the analytic approximation for $M_{\mathrm{CM}},N_{\mathrm{CM}}$, then equation (8) must be solved numerically using the more complicated equations of Appendices A and B of Paper I. Alternatively, equation (8) can be solved approximately by graphical means with relative ease. This is carried out simply by laying out the synchrone axis, along with the normals to the axis at various points with known values of $1-\mu$. From this, the value of $1-\mu$ for that normal containing a given grid point can be determined by interpolation.

3. Next, one must determine which grid points are actually within the differential synchrone tail, which has a width $2v_i\tau$. If the normal distance from the synchrone axis to a grid point is greater than $v_i\tau$, there is no contribution to the density at this grid point for this differential synchrone tail. Thus, for all grid points for which

$$(M_0-M_{\mathrm{CM}})^2+(N_0-N_{\mathrm{CM}})^2\leq v_i^2(1-\mu,\tau;t_c)\tau^2\,, \tag{9}$$

there is a contribution to the density. Here the values of $1-\mu$ for each $M_0,N_0$ which were determined in step 2 must be used in calculating the values of $M_{\mathrm{CM}},N_{\mathrm{CM}}$ and $v_i$. This step can also be carried out approximately by graphical methods. Along each of the normal lines drawn in the previous step, each having a known value of $1-\mu$, the distances $v_i(1-\mu,\ \tau;\ t_c)\tau$ can be laid out in both directions from the axis and the resulting points on either side of the axis on different normal lines connected by a line giving the "edge" of the tail. Those grid points lying within the differential tail can then be determined by inspection.

4. The integrand of equation (7) may now be evaluated for each of the grid points found in step 3. At each grid point, the value of $1-\mu$ found in step 2 may be used to evaluate $f(1-\mu)$ and $dx/d(1-\mu)$. To determine $dx/d(1-\mu)$, which was defined in equation (4a), one must combine equations (3) and (4a) or use the more exact orbit-mechanical relations. The emission rate $\dot{N}_d(t)$ is evaluated at the value of $\tau$ under consideration, using $t=t_c-\tau$. The value of the integrand is then multiplied by the step size $\Delta\tau$.

5. Steps 1–4 may then be repeated for successive values of $\tau$, adding together the contributions for each grid point. In such a procedure, the accuracy involved at a given grid point is of the order of the reciprocal of the number of tails (or $\tau$ values) that actually contribute to the density at that point.

The procedure for the syndyne approach for the calculation of surface density, which was used for $\tau>2\times10^6$ sec on April 27.8 for Comet Arend-Roland, is similar to that just described. Essentially the roles of $1-\mu$ and $\tau$ are reversed, and the modified surface density is given by

$$D=\int_{(1-\mu)_a}^{(1-\mu)_b}\dot{N}_d f(1-\mu)\left[2v_i\tau\frac{dx}{d\tau}(\tau;1-\mu,t_c)\right]^{-1}d(1-\mu)\ , \tag{10}$$

1968ApJ...154..353F

where $dx/d\tau$ is defined by equation (4b). Analogously to equation (8), the equation for the normal containing the point $M_0, N_0$ is

$$-\frac{\partial N_{\mathrm{CM}}/\partial\tau}{\partial M_{\mathrm{CM}}/\partial\tau} = \frac{M_0 - M_{\mathrm{CM}}}{N_0 - N_{\mathrm{CM}}} . \tag{11}$$

As mentioned above, no convenient approximate analytic expression in $\tau$, valid over a large range of $\tau$ values, is available for $M_{\mathrm{CM}}, N_{\mathrm{CM}}$. For the calculations to be presented, the manner in which the $\tau$ integration has been split up requires that no contributions to the density for $\tau < 2 \times 10^6$ sec be included in the syndyne calculations, to avoid double counting with the synchrone calculations used for that range.

The functional parameters determined by comparison with observations of Comet Arend-Roland are shown in Figures 2–4. Consideration of the manner of selection of these functions, their uniqueness, and the dependence of the calculated density distributions upon them will be deferred to the next section. It was pointed out in Paper I that the determination of the absolute level of $\dot{N}_d(t)$ involves certain assumptions regarding dust-particle properties, such as mass density and albedo. We therefore first give $\dot{N}_d(t)$ on a relative basis, denoted by $(\dot{N}_d)_{\mathrm{rel}}$, where this quantity is dimensionless. The estimation of the dimensional constant by which the values of $(\dot{N}_d)_{\mathrm{rel}}$ shown in Figure 2 must be multiplied to yield the actual production rates in dust particles per second will be taken up in § IV. The discontinuous, or step, changes in $(\dot{N}_d)_{\mathrm{rel}}$ were taken purely for calculational convenience. The actual distribution will, of course, be smooth except for the large outburst shown at $t = -0.5 \times 10^6$ sec, which will be discussed below.

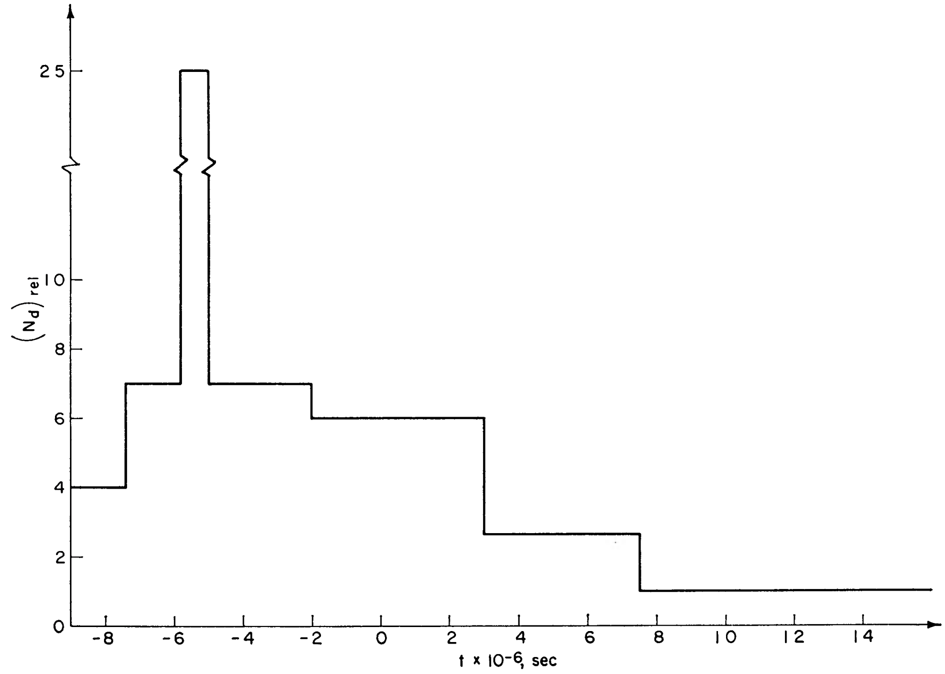

FIG. 2 —Relative dust-particle emission rate $\dot{N}_d(t)$

The particle-size distribution function $f(1 - \mu)$, shown in Figure 3, gives the fraction of particles weighted by their light-scattering ability in a differential $1 - \mu$ range and is normalized to unity. The dashed line shown there represents a somewhat different size-distribution function, which was used for the particles emitted during the outburst.

© American Astronomical Society • Provided by the NASA Astrophysics Data System

1968ApJ...154..353F

This permitted a slightly better comparison of the calculated and measured density distributions.

The function giving the initial particle velocity, $v_i(1-\mu, t)$, was taken for convenience to be the product of two functions—one the function of $1-\mu$ shown in Figure 4, *a*, and the other the time function shown in Figure 4, *b*. The particle-velocity function will be discussed in detail in § IV, when the emission velocity is related to head-gas flow rates.

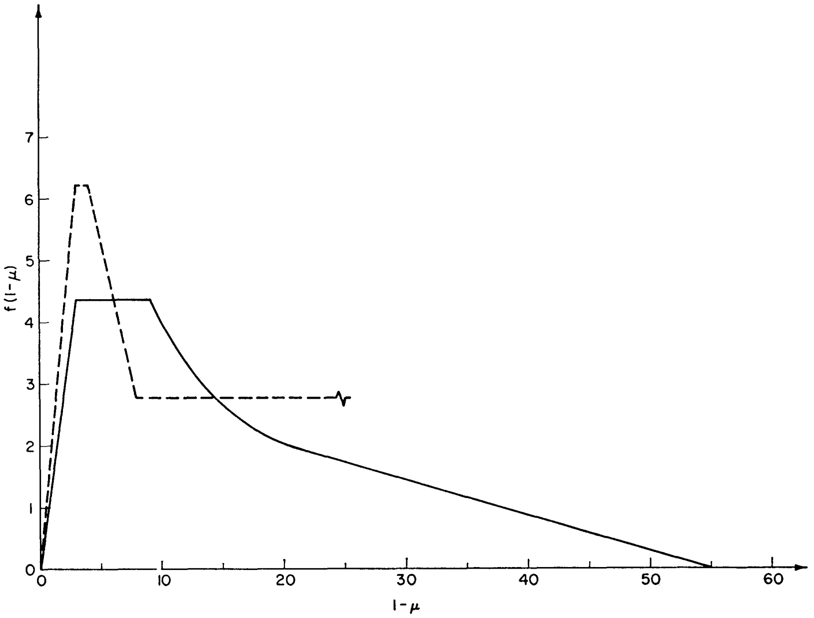

FIG 3 —Particle-size distribution function $f(1-\mu)$

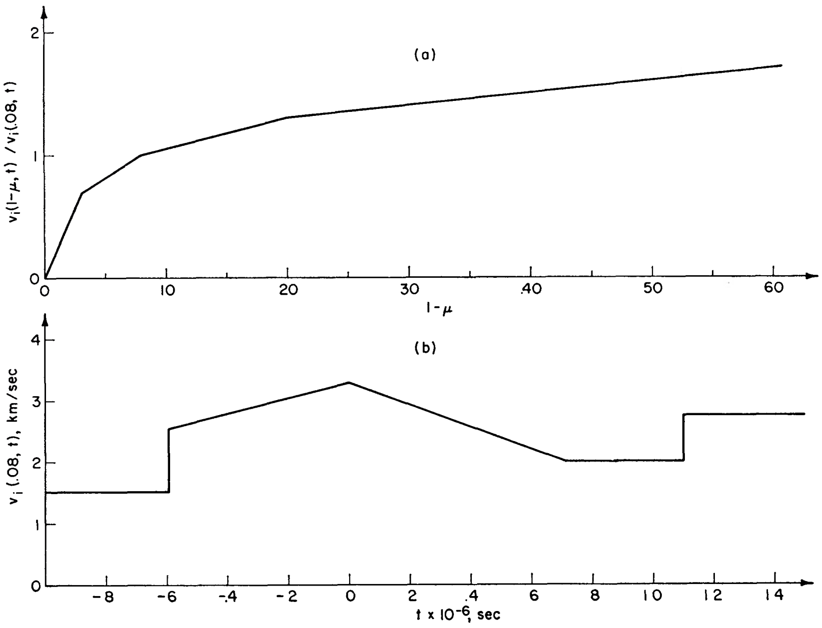

FIG. 4.—Initial-particle-velocity function $v_i(1-\mu, t)$

© American Astronomical Society • Provided by the NASA Astrophysics Data System

1968ApJ...154..353F

Figures 5–8 give the calculated modified surface-density distributions and observed light-intensity distributions for Comet Arend-Roland for the four dates listed in Table 1. In the integrations, 100–200 steps were used, and the densities were obtained at about 300 grid points for each date. The measured light-intensity distributions, shown by the dashed lines, were obtained by Ceplecha (1958) from a microdensitometer analysis of negatives exposed through an orange filter that excludes the blue $CO^+$ emission bands. Thus, while a certain amount of $CO^+$ has been observed to be present in the tail of this comet, the measured light intensities used here result solely from the dust component.

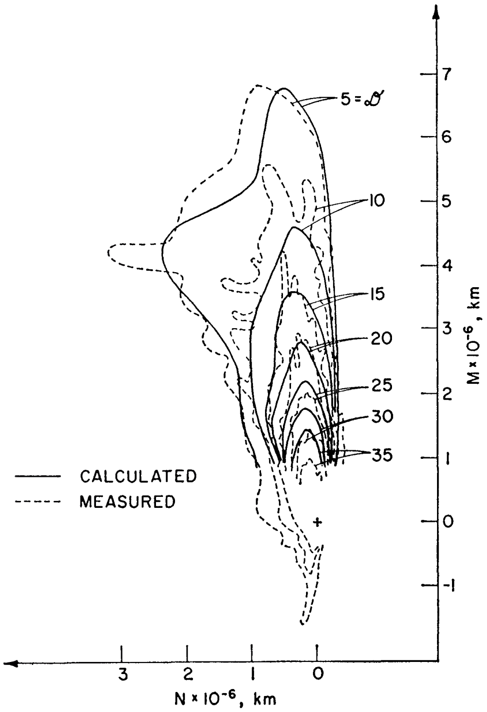

FIG. 5

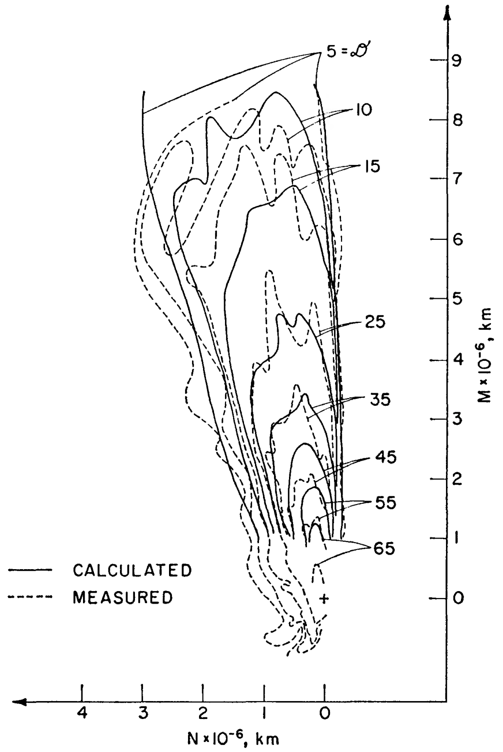

FIG 6

FIG. 5.—Calculated and measured (Ceplecha 1958) isophotes for Comet Arend-Roland on April 27.8, 1957.

FIG. 6.—Calculated and measured (Ceplecha 1958) isophotes for Comet Arend-Roland on April 29.9, 1957.

A second set of measurements on April 27, which were taken only about an hour before those of Figure 5 and which are similar to those of Figure 5, is not shown here. A set of isophotes for April 29.1 was also obtained by Ceplecha, but the measurements are of much shorter extent, since on that night it apparently was not possible to take a sufficiently long exposure for the far tail region. The measured tail extended only to about $2 \times 10^6$ km from the nucleus, and these results are not reproduced here.

The measured isophotes are lines of constant light intensity, and the numbers indicated for the individual isophote curves may be related to the light intensity $I$ by

$$I \propto 10^{0.01\mathfrak{D}} - 1 , \qquad (12)$$

where the $\mathfrak{D}$ values shown in Figures 5–8 are taken directly from Ceplecha's results. Here $\mathfrak{D}$ represents the percentage difference between the value of $\log_{10} I$ at the measured

© American Astronomical Society • Provided by the NASA Astrophysics Data System

1968ApJ...154..353F

point on the photographic plate and that of the background region of the plate. The constant of proportionality in equation (12), which is different for the various dates of observation, depending on the exposure time, will be discussed later when the absolute level of $\dot{N}_d$ is taken up. A $\mathfrak{D} = 0$ level, also given by Ceplecha, is not reproduced in Figures 5–8, as it represents only the limit of detectability against the background fogging of the photographic plate. In addition, some curves for other values of $\mathfrak{D}$ on April 29.9, when a relatively long exposure was made, have been omitted here, for the sake of clarity. The "forward spike" of the comet is evident in the isophotes on April 27.8 and 29.9, and the isophotes for these regions have been included here. No such features are evident in Ceplecha's figures for May 1.9 and May 2.9, and in general the isophotes very near the nucleus have not been reproduced in Figures 5–8, again for the sake of clarity.

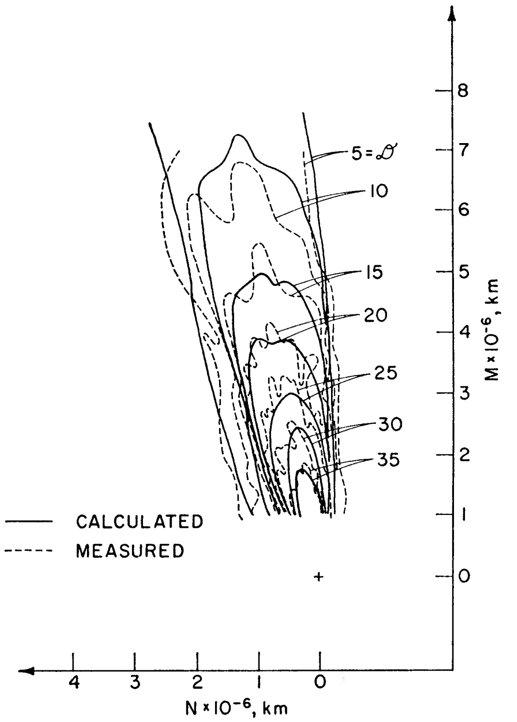

FIG 7

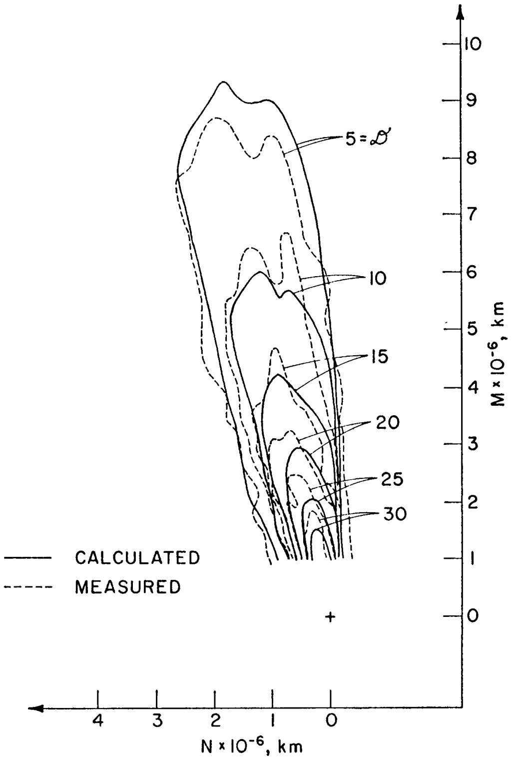

FIG 8

FIG. 7.—Calculated and measured (Ceplecha 1958) isophotes for Comet Arend-Roland on May 1.9, 1957.

FIG. 8.—Calculated and measured (Ceplecha 1958) isophotes for Comet Arend-Roland on May 2.9, 1957.

Information given by Ceplecha relating the angular coordinates of positions in the sky to positions on the isophote plots has been used to fix the $M,N$ coordinates on the figures. The length scale in the $(M,N)$-plane is simply the Earth-comet distance, $\Delta$, times the given angular scales, since the field of the figures is only a few degrees. The apparent radial direction, the $M$-axis, was oriented by determining the angular position of the Sun in the sky on the various dates and using straightforward spherical trigonometry. In this regard, an apparent discrepancy for the last date of observation, May 2.9,

© American Astronomical Society • Provided by the NASA Astrophysics Data System

should be mentioned. Using the information given by Ceplecha, we deduce the $M$-axis to be inclined at an angle of 14°–15° to the apparent tail axis, which is a much larger angle than those for the three earlier dates. While this apparent angle may be expected to increase during the period of Ceplecha's observations, as the Earth becomes more distant from the comet orbit plane, this tail orientation appears to be far out of line with the first three values and cannot possibly be explained in a manner consistent with the data on the earlier dates. Two other isophote diagrams by Ceplecha at the same time, one for a blue filter and one for integral light, give this same angle of 14°–15°. However, the apparent tail angle on this date has been quoted by Brandt and Belton (1966), based on the observations of Beyer and Maffei, to be no more than 10°. Also, an angle of 10° for the same date has been deduced from integral light isophotes, similar to those of Ceplecha but for the near tail region of this comet, by Růžičková and Plavec (1958). For these reasons, it is concluded that an error exists in the information quoted by Ceplecha for this date. The measured isophotes shown in Figure 8 have therefore been rotated $\approx 5°$ clockwise, toward the $M$-axis, to correct this discrepancy.

A minor concern connected with the use of Ceplecha's data is that the axis of Ceplecha's instrument was directed to a point somewhere in the middle of the tail and not at the nucleus of the comet. Strictly speaking, the $(M,N)$-plane should be tangent to the celestial sphere at this point in the tail rather than at the nucleus, as is the case here. However, since the angular difference involved is only 2°–3°, the errors involved are small.

Since we are here concerned only with relative values of $\dot{N}_d$, the level of the calculated densities has been arbitrarily adjusted in Figures 5–8 for optimum agreement. That is, the calculated densities have been set equal to the measured values at a point in the middle region of each of Figures 5–8. This has been done separately for each of the four figures, although strictly speaking it should have been done on only one figure, with the calculated density levels on the other three dates related to those of the first date. However, this would have involved considerations of the constant of proportionality in equation (12), through which a large uncertainty is introduced in the process of calibrating the absolute level of the measured light intensity. This question will be discussed in § IV, where it will be shown that no inconsistency results from fixing the levels of the calculated values separately for each of the four dates.

In the isophote diagram of Figure 5, one cannot help noticing the prominent "bulge" on the left side of the measured isophotes. This feature is also apparent on the measurement, not reproduced here, taken by Ceplecha about an hour earlier on the same night. By comparing the synchrone curves of Figure 1, *a*, with the position of this feature, it is noted that there is a close correspondence with the synchrone for $\tau = 2.25 \times 10^6$ sec. This value of $\tau$ corresponds to $t = -0.54 \times 10^6$ sec, which would be April 2, about 6 days before perihelion. This comparison is the basis for the "outburst" of emission shown in Figure 2. Comparison of Figure 1, *b*, with the measured isophotes of Figure 6 for April 29.9, where the appropriate $\tau$ value is now $2.43 \times 10^6$ sec, again suggests this outburst, although less strongly. Since the improving projection effects on the last two dates (the outburst corresponds to $\tau = 2.60 \times 10^6$ sec on May 1.9 and $\tau = 2.69 \times 10^6$ sec on May 2.9) cause the synchrones for the various $\tau$ values near that of the outburst to be less spread out, the effects of the outburst are not so plainly evident. This outburst is not to be confused with the emission giving rise to the forward spike of this comet, which we will show below to have occurred at very much earlier times.

It is not possible to resolve the exact variation of $(\dot{N}_d)_{\text{rel}}$ during the outburst, and only the total emission involved in the outburst (i.e., the area under the $(\dot{N}_d)_{\text{rel}}$ curve for the outburst) is well determined. For numerical convenience, the duration of the outburst was taken to be $0.8 \times 10^5$ sec (almost 1 day) but could have been significantly less. It could not, however, have extended over a much longer period of time, since no effects of the outburst are evident in Figure 5 at the locations corresponding to those

1968ApJ...154..353F

of the synchrones for $\tau = 2.15 \times 10^6$ sec ($t = -0.44 \times 10^6$ sec) or $\tau = 2.35 \times 10^6$ sec ($t = -0.64 \times 10^6$ sec) in Figure 1, *a*. Also, with regard to the discontinuous rise of $v_i(0.08,t)$ at $t = -0.58 \times 10^6$ sec in Figure 4, *b*, it can only be said that the emission velocity of the particles emitted during the outburst appears to be the higher value, while the particles emitted at earlier times were deduced to have the lower velocities. It is not possible, however, to resolve the exact nature of the change, which one might suspect to be due to greatly increased head-gas emission concurrent with the outburst of dust. We would note here that the discontinuities in $(\dot{N}_d)_{\rm rel}$ connected with the outburst violate the assumption of Paper I that $\dot{N}_d$ be reasonably smooth, as required for use of the syndyne approach. However, sample calculations by the synchrone approach, which avoids this difficulty, were compared with the syndyne calculations used for April 27.8, and it was found that the effects of the discontinuities were small.

As has already been pointed out, a slightly different particle-size distribution function was used for the particles emitted during the outburst. This is shown by the dashed line in Figure 3. The line is terminated at $1 - \mu \approx 0.23$, since particles with larger values of $1 - \mu$ (i.e., smaller particles) had already been removed from the observed tail regions at the above times of observation. The use of such a function permitted a slight improvement in the comparison of the calculations and the measurements in certain respects, such as the density variation along the tail axis on the last two dates.

In the isophotes of Ceplecha for April 27.8, a "forward spike" pointing nearly in the $-M$ direction is evident. Remnants are also apparent on April 29.9, although not so spectacularly. The measured isophotes for May 1.9 and 2.9 in the region of the nucleus, which are not reproduced here, show no definite traces of this feature. It has been pointed out (see, e.g., Öpik 1958) that this forward spike consists of particles emitted at exceedingly low velocities early in the passage of the comet past the Sun. These particles are located almost entirely in the comet orbit plane and because of the Earth's position close to this plane appear as a forward spike.

We may compare the measured isophotes of the forward spike in Figure 5 with the synchrones of Figure 1, *a*, for very large values of $\tau$. The comparison suggests that the emission of the dust particles in the spike occurred for $\tau$ values in the range 5–7 $\times 10^6$ sec. On April 29.9 the corresponding $\tau$ range is 5.2–7.2 $\times 10^6$ sec, which again may be seen to agree well with the position of the measured traces of the spike. The corresponding range of emission times would be $t = -3.3$ to $-5.3 \times 10^6$ sec which, since perihelion was on April 8, 1957, corresponds to the range of March 1, 1957, to February 6, 1957. On March 1 the heliocentric distance was $r_c \approx 1.02$ a.u., and on February 6 it was $r_c \approx 1.45$ a.u.

In Paper I it was shown that in the limit $v_i \rightarrow 0$, equation (7) or equation (10) reduces to the simple form

$$D = \dot{N}_d f(1-\mu)\left[\left|\frac{\partial M_{\rm CM}}{\partial(1-\mu)}\frac{\partial N_{\rm CM}}{\partial\tau} - \frac{\partial M_{\rm CM}}{\partial\tau}\frac{\partial N_{\rm CM}}{\partial(1-\mu)}\right|\right]^{-1} . \qquad (13)$$

This expression could be used for the calculation of the density distribution in the region of the forward spike. However, the extreme crowding of the synchrones, coupled with the rather small scale, results in insufficient resolution to permit a meaningful calculation of detailed isophotes in this region.

Sample calculations have been carried out for one point in the forward spike for the dates April 27.8 and 29.9. The maximum extension of the isophotes in the spike region would appear to be oriented most nearly with a synchrone for $t = -4.3 \times 10^6$ sec, which is in the middle of the range $t = -3.3$ to $-5.3 \times 10^6$ sec quoted above. On April 27.8, at the position of maximum distance from the nucleus of the $\mathfrak{D} = 5$ line in the spike region, the value of $1 - \mu$ is about 0.017, and the Jacobian in equation (13) has a value of $0.277 \times 10^7$ km$^2$ sec$^{-1}$. The calculated surface density at this point has the

© American Astronomical Society • Provided by the NASA Astrophysics Data System

same value as that of the calculated $\mathfrak{D} = 5$ line in the normal tail on this same date if $(\dot{N}_d)_{\mathrm{rel}} f = 0.076$. Similarly, on April 29.9, again for $t = -4.3 \times 10^6$ sec, at the "tip" of the $\mathfrak{D} = 10$ line in the forward spike, it was found that $1 - \mu = 0.015$, and the Jacobian was found to be $0.49 \times 10^7$ km$^2$ sec$^{-1}$. Matching this to the calculated value of the $\mathfrak{D} = 10$ level in the normal tail on this date gives $(\dot{N}_d)_{\mathrm{rel}} f = 0.073$, which is remarkably consistent with the value for April 27.8. If we assume that the same particle-size distribution function holds for the particles in the forward spike as for those particles in the normal tail, so that the solid line in Figure 3 may be used for $f(1 - \mu)$, we then get

$$(\dot{N}_d)_{\mathrm{rel}} \approx 0.03 \quad \text{at} \quad t = -4.3 \times 10^6 \text{ sec} \tag{14}$$

on the scale of Figure 2. This value is to be taken to be the maximum rate of emission for the particles of the forward spike, and the emission of these particles extends in time at least $10^6$ sec before and after the above time at diminished rates.

The reader may form his own conclusions regarding the quality of the comparison between the calculated and observed isophotes of Figures 5–8. It is noted, however, that not only the basic features of the observations are reproduced by the calculations, but also a great many of the smaller details such as certain of the "wiggles." Nowhere in these tails is the difference between the measured and calculated densities greater than 10–20 per cent, which is probably less than the uncertainties inherently associated with microdensitometer measurements of photographic plates in astronomical applications.

## III. DEPENDENCE OF SURFACE DENSITY ON FUNCTIONAL PARAMETERS

In this section we consider the manner in which the modified surface-density distributions depend on the comet functional parameters $f(1 - \mu)$, $\dot{N}_d(t)$, and $v_i(1 - \mu, t)$. In so doing, the choice of the functions presented in the previous section will be justified. The questions of the uniqueness of the selection of the functions and the sensitivity of isophote forms to changes in the functions will also be considered. The procedure by which the comet functional parameters may be deduced from observational data in general (i.e., for comets other than Comet Arend-Roland) may be inferred from the present discussion.

Certain very general features of the dependence of surface-density distributions on the functional parameters may be deduced by inspection of the syndyne-synchrone loci of Figure 1. We would first note that for the velocity function $v_i(1 - \mu, t)$ shown in Figure 4, $v_i \sim 0.3$ km sec$^{-1}$, so that the widths of the differential syndyne or synchrone tails, $2v_i\tau$, are of the order of $10^6$ km. When this distance is compared with the distances between the various syndynes or synchrones of Figure 1, a certain, but limited, amount of overlap between the various differential tails is evident. Since this overlap is not too large, it can be said that the density at points near the $M$-axis is due to particles emitted at late times (i.e., small $\tau$ values), while the density at large distances from the $M$-axis results from early emissions. From this it can be concluded that the non-radiality of the tail would increase if the relative amount of emission at early times were increased. Similarly, since $1 - \mu$ increases monotonically along any particular synchrone, it would appear that the particle-size distribution function $f(1 - \mu)$ has a large effect on the variation of the density in the axial direction. Increasing the value of $f(1 - \mu)$ at larger values of $1 - \mu$ would tend to increase the relative density in the far tail region, while a relative increase of $f(1 - \mu)$ at small values of $1 - \mu$ would increase the density in the near tail region.

In order to define in a more precise manner the nature of the various dependences, a number of modified surface-density distributions have been calculated for Comet Arend-Roland on the four dates considered above, for functional forms of $f(1 - \mu)$, $\dot{N}_d(t)$, and

$v_i(1-\mu, t)$ other than those given in § II. The resulting surface-density distributions may be approximately characterized by four quantities:

*a*) *The apparent tail angle,* i.e., the angle between the tail axis in the $(M,N)$-plane and the $M$-axis, which serves as a measure of the tail orientation.

*b*) *The half-width of the tail,* taken in the middle region of the tail, which serves as a measure of the cross-sectional shape.

*c*) *The relative density in the far tail region,* expressed by the ratio of the density on the tail axis at an appropriately defined location in the far tail to the density on the tail axis in the middle tail region.

*d*) *The relative density in the near tail region,* measured in a manner analogous to that for the far tail.

The behavior of the above four quantities with changes in the three functional parameters has been studied by successively varying each function with the remaining two functions held fixed at their "optimal" form. The optimal functions denoted by $f^{(0)}$, $\dot{N}_d^{(0)}$, and $v_i^{(0)}$ are the functions shown in Figures 2–4, upon which the calculated isophotes of Figures 5–8 are based.

Six functional forms were investigated for the particle-size distribution $f(1-\mu)$. These functions are denoted by $f^{(1)}$ to $f^{(6)}$ and are shown in Figure 9, where for comparison the optimal function $f^{(0)}$ is also shown. Similarly, Figure 10 shows the six functions $\dot{N}_d^{(1)}$ to $\dot{N}_d^{(6)}$ considered for the relative dust-particle emission rate, where the subscript "rel" has been omitted for clarity. The outburst discussed in § II was considered a sufficiently well-established feature that it was included in each of the six functions. In considering the variations of the density distributions with $v_i(1-\mu, t)$, changes in the dependence of $v_i$ on $1-\mu$ were not investigated, since this dependence was assumed to be determined from the inner-head-flow solution discussed in Paper I. Figure 11 shows the five forms of the time dependence of $v_i$ which were investigated, along with the optimal form.

In order to characterize the functions given, appropriate moments or averages were used. The particle-size functions were characterized by two quantities, one measuring the fraction of particles in the relatively high $1-\mu$ range $(0.1 \lesssim 1-\mu \lesssim 0.3)$ and the other the fraction of particles in the low $1-\mu$ range $(0 < 1-\mu \lesssim 0.03)$. The dust emission rate was characterized by the average time of emission over the time range shown in Figure 10. The behavior of the emission velocity with time was described by two quantities. One quantity was the time-averaged value of $v_i$ over the same time range used for $\dot{N}_d$. The other quantity, the ratio of the average value of $v_i$ in the last half of this time range to that in the first half, measures the asymmetry of the time dependence of $v_i$.

The behavior of the four parameters characterizing the isophotes has been investigated as a function of the above averages calculated for the different functional forms shown in Figures 9–11. The details of this study may be found in Finson and Probstein (1967). We here summarize the essential results:

*a*) The tail orientation is a strong function of $f(1-\mu)$, $\dot{N}_d(t)$, and $v_i(1-\mu, t)$. The tail angle increases for functions $f(1-\mu)$ which have a greater concentration of particles at low values of $1-\mu$ (i.e., large particles), for forms of $\dot{N}_d$ which have greater emissions at early times, for a general increase in the level of $v_i$, and for asymmetrical time variations of $v_i$ which have lower velocities at early emission times and higher velocities at late times.

*b*) The width of the tail is primarily dependent on $v_i$, being greater for higher levels of $v_i$ and, to a somewhat lesser extent, being decreased for asymmetrical time variations of $v_i$.

*c*) The variation of the density along the tail axis is almost solely a function of $f(1-\mu)$. The rate of decrease of the density in the axial direction increases with a more rapid decrease of $f$ with $1-\mu$.

© American Astronomical Society • Provided by the NASA Astrophysics Data System

1968ApJ...154..353F

On the basis of these conclusions, the question of the uniqueness of the selection of the functional parameters given in the previous section can at least be answered *empirically*. It should be clear at this point that no substantial change of any *one* of the three functional parameters can be made without radically altering at least one important feature of the calculated isophotes. Such a change would, of course, preclude the quality of agreement between the measured and calculated isophotes which was obtained. We may, however, ask what the result would be of a simultaneous change in any two or even in all three of the functions. Referring to the above conclusions, we note that any substantial change in $f(1-\mu)$ would give rise to changes in the axial variation of the density, which could be offset only by extremely large changes of one or both of the other two functions. But, since the tail orientation is a strong function of all three functions, it

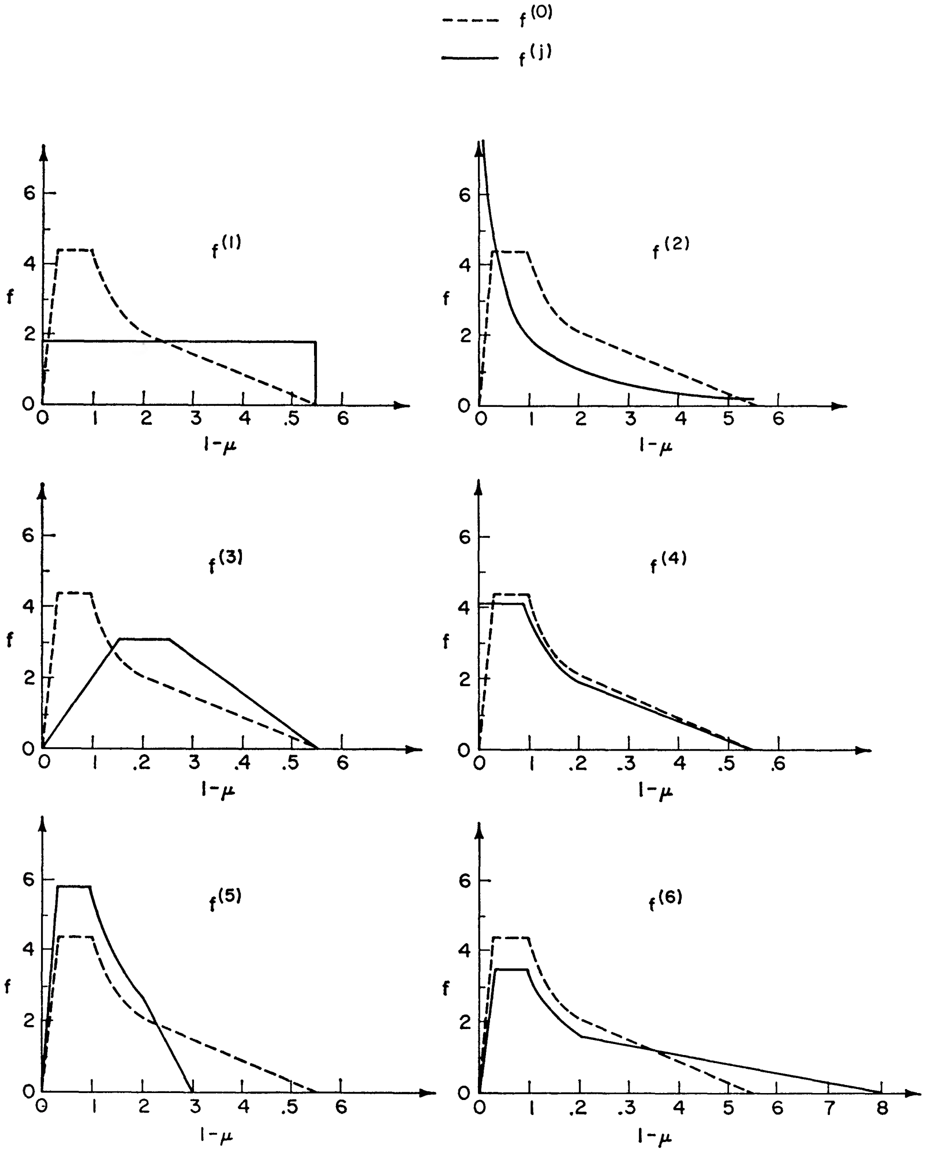

FIG. 9 —Particle-size distribution functions $f^{(i)}$

© American Astronomical Society • Provided by the NASA Astrophysics Data System

1968ApJ...154..353F

would be very drastically altered in such a procedure. Similarly, the emission velocity may be considered to be well determined from considerations of the cross-sectional shapes. Once $f(1 - \mu)$ and $v_i$ have been so determined, only $\dot{N}_d(t)$ may be varied, and this must be done so as to provide the correct tail orientation.

It is to be noted that the above discussion applies only to those ranges of the independent variables, $1 - \mu$ and $t$, which have an effect on the isophote distributions. Excluding the forward spike, for the calculations described for Comet Arend-Roland, particles emitted before $t \approx -1.0 \times 10^6$ sec had essentially been blown out of the observed regions of the tail at the time of observation, and particles emitted after $t \approx +1.5 \times 10^6$ sec had yet to reach the observed tail regions. Thus $\dot{N}_d$ and $v_i$ have been given only for $-1.0 \times 10^6 \leq t \leq +1.5 \times 10^6$ sec. Similarly, particles with $1 - \mu \lesssim 0.03$ or $1 - \mu \gtrsim 0.30$ do not play an important role within the observed tail region, so that $f(1 - \mu)$ should be considered to be reliably determined only in the range $0.03 \lesssim 1 - \mu \lesssim 0.30$.

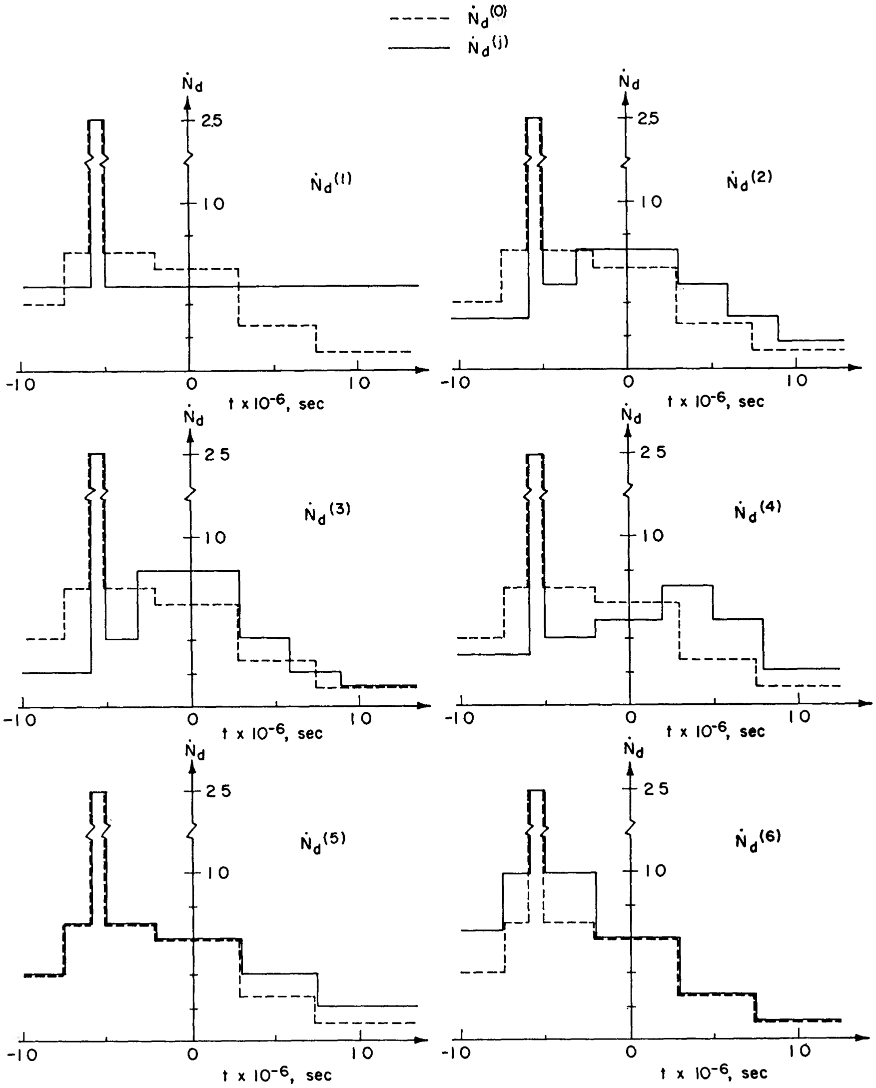

FIG. 10.—Relative dust-particle emission rates $\dot{N}_d^{(j)}$

© American Astronomical Society • Provided by the NASA Astrophysics Data System

For the calculated isophotes shown in Figures 5–8, a high level of agreement with the measured isophotes was desired. To achieve this, it was necessary to take into account finer details not considered above, which have a 10 to 20 per cent effect on the dependence of the density distributions on the functional parameters. We shall not discuss these considerations at any length, since they are of less general interest than the basic description given above. However, it may be noted, for example, that the exact functional forms of the time variation of $\bar{N}_d$ and $v_i$ were deduced from considerations of cross-sectional variations of the density. The "tail" of the particle-size distribution was also deduced from similar considerations. A more extended "tail," as shown in Figure 9 for $f^{(6)}$, gives rise to a somewhat detrimental effect on the relative spacing of the various isophotes on the leading (small $N$) side of the tail, while the opposite change shown by $f^{(5)}$ causes a slightly lower density level in the far tail region on April 27.8.

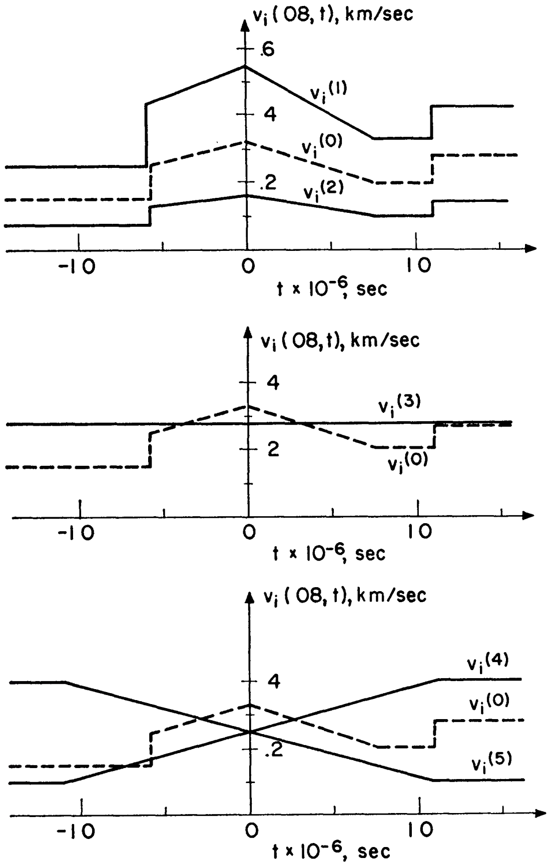

FIG. 11.—Time-dependent portions of initial-particle-velocity functions $v_i^{(j)}$

## IV. DERIVED RESULTS

Following the procedure outlined in Paper I, the determination of the three comet functional parameters discussed in the preceding two sections constitutes the "first stage" of the calculations. We again emphasize here that this first stage required no assumptions regarding the exact nature of the dust particles, the details of the light scattering from the dust particles (other than the validity of eq. [1]), or the precise state of the comet nucleus. In accordance with what was termed the "second stage" in Paper I,

© American Astronomical Society • Provided by the NASA Astrophysics Data System

these functional parameters can now be used to determine other information on dust comets of more direct physical significance by introducing assumptions regarding the light scattering and dust-particle density. We first relate $1 - \mu$ to the product $\rho_d d$ by means of equation (1). In so doing, it is necessary to assume a value for the scattering efficiency $Q_{\mathrm{pr}}$ involved in the constant $C$. As noted in Paper I, $Q_{\mathrm{pr}}$ has a range of about 1–2 for metallic particles and is somewhat less than unity for a dielectric medium. We shall here take $Q_{\mathrm{pr}} = 1$, where this value is understood to be uncertain to within a factor of 2. For this value of $Q_{\mathrm{pr}}$ the constant $C$ in equation (1) is equal to $1.19 \times 10^{-4}$ g cm$^{-2}$.

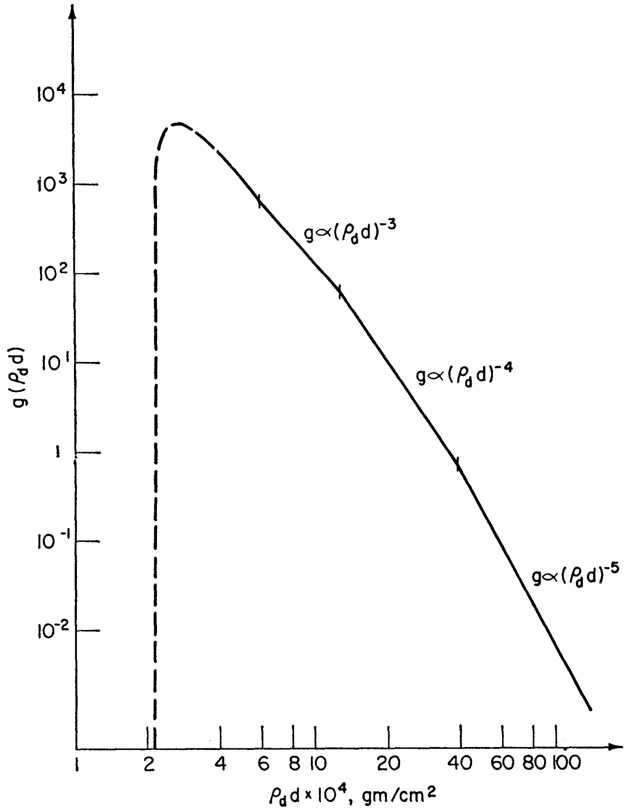

FIG. 12.—Dust-particle-size distribution function $g(\rho_d d)$ ($Q_{pr} = 1$)

Knowing $C$, we can now determine the actual particle-size distribution function $g(\rho_d d)$ introduced in Paper I. This function is related to $f(1 - \mu)$ by

$$g(\rho_d d) = \frac{1}{C}(1-\mu)^4 f(1-\mu) \Big/ \int_0^\infty (1-\mu)^2 f(1-\mu) d(1-\mu) , \tag{15}$$

where

$$\int_0^\infty g(\rho_d d) d(\rho_d d) = 1 . \tag{16}$$

The factor $(\rho_d d)^2$, introduced into the modified particle-size distribution function $f(1 - \mu)$ to take into account the particle cross-sectional area, has been removed from $g(\rho_d d)$.

The particle-size distribution function $g(\rho_d d)$ calculated from equation (15), using $f(1 - \mu)$ given by the solid line in Figure 3, is shown in Figure 12. It should be noted that $g(\rho_d d)$ goes sharply to zero at $\rho_d d = 2.16 \times 10^{-4}$ g cm$^{-2}$ as a result of the fact that $f(1-\mu)$ was taken to be zero for $1-\mu \geq 0.55$. As pointed out in the preceding section, the behavior of $f(1-\mu)$ for $1-\mu \gtrsim 0.30$ does not strongly influence the calculated density distributions, and the "tail" of the distribution function $f(1-\mu)$ cannot be considered to be well determined. Hence the corresponding portion of Figure 12 is denoted by the dashed curve, and no great significance should be attached to this limiting minimum value of $\rho_d d$. What is considered to be reliably determined, however, is the behavior of $g(\rho_d d)$ for $\rho_d d$ values in the range 4–40 × $10^{-4}$ g cm$^{-2}$.

An important value optically of $\rho_d d$ is the root-mean-square value $\langle(\rho_d d)^2\rangle^{1/2}$, where

$$\langle(\rho_d d)^2\rangle = \int_0^\infty (\rho_d d)^2 g(\rho_d d) d(\rho_d d) \, . \tag{17}$$

The root-mean-square value is found to be equal to $5.6 \times 10^{-4}$ g cm$^{-2}$ and is not strongly dependent on the behavior of $g(\rho_d d)$ at the smaller $\rho_d d$ values. Assuming a constant value of $\rho_d$ over all particles, the optically important particle diameter is then 5.6 $\mu$ for $\rho_d = 1$, 1.9 $\mu$ for $\rho_d = 3$, and 0.8 $\mu$ for $\rho_d = 7$ g cm$^{-3}$.

Next we may determine the absolute level of the dust emission rate $\dot{N}_d$. In so doing, it is necessary to consider the amount of light scattered by an individual dust particle in the direction of the Earth. Considerable uncertainty is introduced here. The albedo, the ratio of scattering to extinction, is not well known for the dust particles and may have a value between 0.5 and 0.05. Also, the phase-angle function, giving the amount of light scattered in various directions, is only poorly known. (The phase angle $\alpha$ is the angle between the Sun-comet and Earth-comet lines and was ~90° for Comet Arend-Roland on the dates considered.) We shall define the phase-angle function $\phi(\alpha)$ as the ratio of the light scattered in the direction $\alpha$ to that which would result from isotropic scattering. Then, if $A$ is the albedo and $I_0$ the solar light intensity at 1 a.u. from the Sun, and if we assume that the cross-section for extinction is the geometrical cross-section, the light received by an observer on the Earth from an individual dust particle of diameter $d$ is

$$\frac{I_0 \pi d^2/4}{4\pi\Delta^2} A\phi(\alpha)\left(\frac{1 \text{ a.u.}}{r_c}\right)^2 . \tag{18}$$

Theoretical calculations of $\phi(\alpha)$, based on the Mie theory, are difficult even for such simple shapes as spheres and have not been carried out for irregularly shaped particles Of more interest are laboratory measurements by Richter (1959) of the light scattering from both metallic and dielectric particles of 1-$\mu$ diameter. The scattering was found to be nearly isotropic for dielectric particles, while for metallic particles $\phi(\alpha)$ was only about 0.2 near $\alpha = 90°$. On the basis of these results and of the range given for the albedo, we shall consider the probable range of the product $A\phi(\alpha)$ to be $0.01 \leq A\phi(\alpha) \leq 0.50$. Since the phase angle changed by no more than 20° during the period of Ceplecha's observation of Comet Arend-Roland, $A\phi(\alpha)$ will be assumed constant for the four dates.

In the calculated modified surface densities presented in Figures 5–8 the actual number of particles in the comet tail is multiplied by the factor $(\rho_d d)^2/\langle(\rho_d d)^2\rangle$, so as to be proportional to the light intensity. Since the light intensity would be given correctly if the number of particles had been multiplied by the factor of equation (18), the calculated light intensity per unit area in the $(M,N)$-plane is related to the modified surface density $D$ by the relation

$$I = \frac{I_0 A\phi(\alpha)}{16\Delta^2}\left(\frac{1 \text{ a.u.}}{r_c}\right)^2 \frac{\langle(\rho_d d)^2\rangle}{\rho_d^2} \frac{\dot{N}_d}{(\dot{N}_d)_{\text{rel}}} D \, . \tag{19}$$

1968ApJ...154..353F

Here $I_0$ is in, say, lumens per square meter, while $D$ in this relation is calculated with the dimensionless $(\dot{N}_d)_{\text{rel}}$ in place of the dimensional $\dot{N}_d$ so that $\dot{N}_d D/(\dot{N}_d)_{\text{rel}}$ is in particles per square kilometer. The ratio $\dot{N}_d/(\dot{N}_d)_{\text{rel}}$ is the constant required to transform the relative emission rate of Figure 2 into the actual emission rate and is in particles per second.

Information given by Ceplecha relating the $\mathfrak{D}$ levels of the measured isophotes to the magnitude scale, together with the manner in which the calculated $D$ levels were matched to the $\mathfrak{D}$ levels for the isophote figures, may be used to determine $\dot{N}_d/(\dot{N}_d)_{\text{rel}}$. As pointed out in § II, this matching was done separately for each of the four dates of observation. It is found, for fixed values of $A\phi(\alpha)$ and $\rho_d$, that the value of $\dot{N}_d/(\dot{N}_d)_{\text{rel}}$ is about half as much on the first and last dates as on the middle two. This discrepancy is attributed to the calibration of the level of the measured light, a difficult task for low-intensity light from a diffuse source such as a comet tail. In fact, it may be noted that the light-intensity levels of the two measurements of Ceplecha, which were performed about an hour apart on the night of April 27, differ by a factor of about 2.5, i.e., by about one magnitude. It is difficult to conceive of such a change as being real.

If we use the average of the values for the four dates considered, we find that

$$\frac{A\phi(\alpha)}{\rho_d^2}\frac{\dot{N}_d}{(\dot{N}_d)_{\text{rel}}} = 4.0 \times 10^{16}\ \text{cm}^6\ \text{g}^{-2}\ \text{sec}^{-1}\ , \tag{20}$$

where $\rho_d$ is in grams per cubic centimeter. It is apparent that the value of $\dot{N}_d/(\dot{N}_d)_{\text{rel}}$ can vary considerably, depending on the values assumed for $A\phi(\alpha)$ and $\rho_d^2$. For a probable lower limit we take $\rho_d = 1$ g cm$^{-3}$ and $A\phi(\alpha) = 0.50$, giving $\dot{N}_d/(\dot{N}_d)_{\text{rel}} = 8.0 \times 10^{16}$ particles sec$^{-1}$, while for a probable upper limit we take $\rho_d = 7$ g cm$^{-3}$ and $A\phi(\alpha) = 0.01$, giving $\dot{N}_d/(\dot{N}_d)_{\text{rel}} = 2.0 \times 10^{20}$ particles sec$^{-1}$. Using the values $A\phi(\alpha) = 0.08$ and $\rho_d = 3$ g cm$^{-3}$, corresponding approximately to the middle of the ranges, we have

$$\dot{N}_d/(\dot{N}_d)_{\text{rel}} = 4.5 \times 10^{18}\ \text{particles sec}^{-1}\ . \tag{21}$$

Using this value, from Figure 2 we find the rate of dust production to be $2.7 \times 10^{18}$ particles sec$^{-1}$ at $t = 0$ (perihelion) and $4.5 \times 10^{17}$ particles sec$^{-1}$ at $t = 10^6$ sec. The total number of particles emitted in the outburst at $t \approx -0.5 \times 10^6$ sec is $9 \times 10^{23}$.

The mass production rate of dust $\dot{m}_d$ is given by the product of the number production rate and the average particle mass over the size distribution $g(\rho_d d)$. The latter is given by $\pi\langle(\rho_d d)^3\rangle/6\rho_d^2$, where $\langle(\rho_d d)^3\rangle$ is evaluated in a manner completely analogous to $\langle(\rho_d d)^2\rangle$, defined in equation (17). Note that, since $\dot{N}_d \propto \rho_d^2$, the $\rho_d^2$ factors cancel, and since $\langle(\rho_d d)^2\rangle$ and $\langle(\rho_d d)^3\rangle$ are simply moments of the distribution function $g(\rho_d d)$, they are constants and no dependence on $\rho_d$ remains. Thus, to evaluate $\dot{m}_d$, we need only assume a value for $A\phi(\alpha)$, so that $\dot{m}_d$ is determined with much less uncertainty than is $\dot{N}_d$. The value of $\langle(\rho_d d)^3\rangle$ turns out to be $4.78 \times 10^{-10}$ g$^3$ cm$^{-6}$. With $A\phi(\alpha) = 0.01$, 0.08, and 0.50, the respective values of $\dot{m}_d$ at perihelion are $6 \times 10^8$, $7.5 \times 10^7$, and $1.2 \times 10^7$ g sec$^{-1}$. At late times, say, $t > 0.75 \times 10^6$ sec, the values would be lower by a factor of 6. The respective values for the total mass emitted during the outburst are $2 \times 10^{14}$, $2.5 \times 10^{13}$, and $4 \times 10^{12}$ g.

We now turn to the "third stage" outlined in Paper I and determine the production rate of the comet head gas from the dust mass flow rates and the dust-particle emission velocities $v_i$ given in Figure 4. To do this, we use the results of Probstein (1968) for the emission velocity of the dust particles from the inner head region. These results are summarized in Figure 13, where

$$\mathfrak{M} = \dot{m}_d/\dot{m}_g \qquad \beta = \tfrac{16}{3}\pi\rho_d d r_0 (c_p T_{g_0})^{1/2}/\dot{m}_g\ . \tag{22}$$

© American Astronomical Society • Provided by the NASA Astrophysics Data System

Here $\dot{m}_g$ is the mass flow rate of the neutral head gas, $r_0$ the nucleus radius, $T_{g_0}$ the temperature of the head gas at the nucleus, and $c_p$ the specific heat of this gas. While $\dot{m}_g(t)$ can in principle be determined at all times from the time variation of $v_i$ and $\dot{m}_d$, the process is sufficiently complicated that we shall here determine $\dot{m}_g$ only at a few selected times.

The evaluation of $\dot{m}_g$ will be carried out for particles with $1 - \mu = 0.08$ or (with $Q_{\rm pr} = 1$) $\rho_d d = 14.9 \times 10^{-4}$ g cm$^{-2}$. At this value the $1 - \mu$ part of the initial-particle-velocity function $v_i$ has a value of 1. This part of $v_i$ was chosen to have nearly the same slope as the curves in the region of interest in Figure 13, so that approximately the same values of $\dot{m}_g$ would result if other values of $\rho_d d$ were used. A nucleus radius of $r_0 = 5$ km will be assumed, and a nucleus temperature $T_{g_0} = 200°$ K. With the head-gas specific heat $c_p$ taken as that of a perfect gas with 5 degrees of freedom and a molecular weight of 25, $(c_p T_{g_0})^{1/2} \approx 0.49$ km sec$^{-1}$. From these values we have

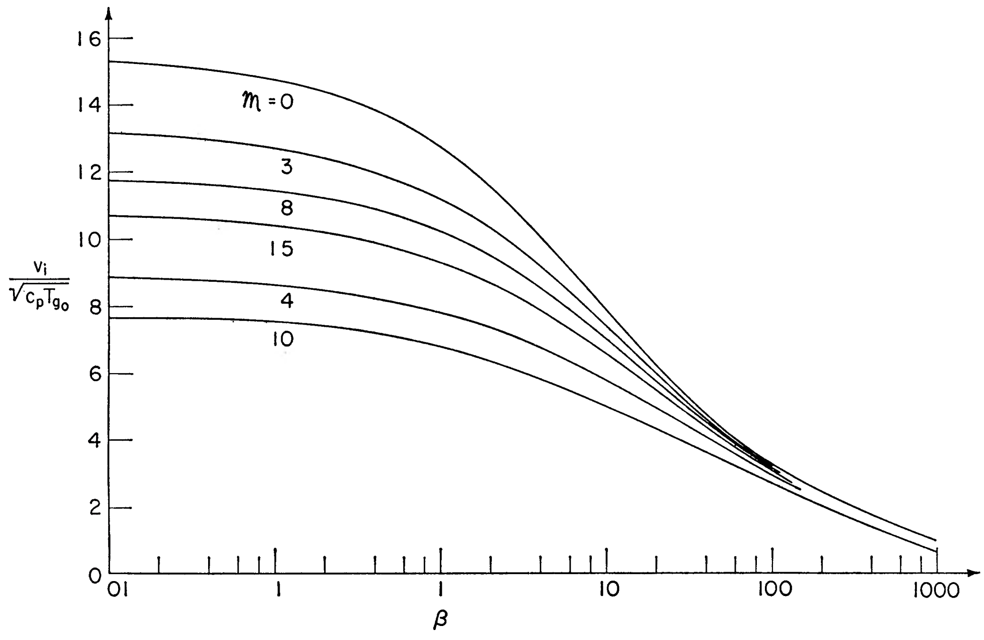

FIG. 13.—Emission speed of dust particles from inner head region (Probstein 1968)

$$\beta \dot{m}_g = 6.1 \times 10^8 \text{ g sec}^{-1} . \tag{23}$$

As a specific example, let us find $\dot{m}_g$ at the time of perihelion, when $v_i(0.08,t)$ had its maximum value of 0.33 km sec$^{-1}$, so that $v_i/(c_p T_{g_0})^{1/2} \approx 0.67$. With the mass production rate of dust at perihelion given above for $A\phi(a) = 0.08$,

$$\mathfrak{M} \dot{m}_g = 7.5 \times 10^7 \text{ g sec}^{-1} . \tag{24}$$

Thus in this case $\beta \approx 8\mathfrak{M}$. From Figure 13 along the line $v_i/(c_p T_{g_0})^{1/2} = 0.67$, we see that $\beta \approx 8\mathfrak{M}$ at $\beta \approx 10$. Thus, from equation (23), $\dot{m}_g \approx 6 \times 10^7$ g sec$^{-1}$ at perihelion.

This procedure has been carried out for $A\phi(a) = 0.01$, 0.08, and 0.50 and at the times $t = -0.8 \times 10^6$, $t = -0.54 \times 10^6$ (during the outburst), $t = 0$, and $t = +1.0 \times 10^6$ sec. The resulting values of $\dot{m}_g$ are given in Table 4. $T_{g_0} = 200°$ K and $r_0 = 5$ km were used in all cases. It is apparent from Table 4 that $\dot{m}_g$ is not particularly sensitive to the mass production rate of dust $\dot{m}_d$. A change of $A\phi(a)$, and hence also $\dot{m}_d$, by a factor of 50 results in a much smaller change in $\dot{m}_g$. This may be attributed to the relative closeness of the lines $\mathfrak{M}$ = constant in the vicinity of $\mathfrak{M} = 1$, so that at a given value of $v_i$ a small range of possible $\beta$ values results. Since $v_i$ was determined directly from comparisons with measured isophote distributions, the only significant uncertainty remaining is in connection with the nucleus radius $r_0$, to which $\dot{m}_g$ is essentially proportional. The uncertainty in the initial gas temperature $T_{g_0}$ is much less important, since it is known to within a factor of 2 and, furthermore, only the square root of this quantity enters in applying the results of Figure 13.

## V. COMPARISON OF RESULTS WITH PREVIOUS ESTIMATES

Let us now compare the results obtained with those of other investigators. Most of the more detailed results, such as the isophote figures of § II and the various functional parameters, are obtained here for the first time. As a result, many of the comparisons must necessarily be in terms of less detailed, order-of-magnitude considerations.

TABLE 4

VALUES OF $\dot{m}_g$ IN GRAMS PER SECOND

| $t\times10^{-6}$ (sec) | $A\phi(a)$ | | |
|---|---|---|---|
| | 0 01 | 0.08 | 0 50 |
| $-0.80$... | $2\times10^{7}$ | $8\times10^{6}$ | $6\times10^{6}$ |
| $-0\ 54$.... | $1\ 5\times10^{8}$ | $5\ 5\times10^{7}$ | $2\ 7\times10^{7}$ |
| 0........ | $1\ 5\times10^{8}$ | $6\ 0\times10^{7}$ | $4\ 6\times10^{7}$ |
| $+1\ 00$. . . | $1\ 7\times10^{7}$ | $1\ 2\times10^{7}$ | $1\ 0\times10^{7}$ |

The only aspect of the above isophote calculations which may be compared with a previous study is the forward spike of Comet Arend-Roland. Öpik (1958) analyzed this feature from observations made on April 25, 1957, the very date on which the Earth passed through the comet orbit plane, when the spike appeared to be very thin and to point directly toward the Sun. From the observed narrowness of the spike, he concluded that the particles in the spike were emitted from the nucleus (in terms of the present model, from the inner head region) at very small velocities and that it was doubtful that any forces other than solar gravity and radiation pressure acted on the particles. Analyzing the motion of these particles after their emission, he showed that emission would have to have occurred no later than April 2, 1957, or else the spike would not have been projected in the forward direction. These conclusions are all consistent with the results of the present study. However, he then assumed that the emission did not take place very much earlier than April 2, between March 29 ($t \approx -0.8 \times 10^6$ sec) and April 2 ($t \approx -0.5 \times 10^6$ sec), a period very different from that of February 6–March 1 deduced in § II. With reference to the synchrones of Figure 1, *a*, *b*, and the measured isophotes of Figures 5 and 6, we would note that the emission dates deduced by Öpik are inconsistent with the observed positions of the spike on dates other than April 25.

No previous direct estimates are available for the comet functional parameters $\dot{N}_d(t)$, $\dot{m}_g(t)$, and $f(1-\mu)$ or $g(\rho_d d)$, except that functions similar to our $g(\rho_d d)$, but expressed in terms of $d$ alone, were suggested by Remy-Battiau (1964) and Öpik (1958). If $\rho_d$ is

© American Astronomical Society • Provided by the NASA Astrophysics Data System

constant for all particles, this difference is immaterial, and we shall call such a function $g(d)$. Size distributions of the form

$$g(d) \propto d^{-k} \tag{25}$$

were investigated. The study of Remy-Battiau (1964) of the continuous spectrum from the heads of Comets Arend-Roland and Mrkos indicated a likely value of 4 for $k$, with a lower limit for the particle size of $d = 10^{-6}$ cm. This distribution is seen to be qualitatively similar to the behavior of $g(\rho_d d)$ shown in Figure 12, in the range $4 \times 10^{-4} \leq \rho_d d \leq 40 \times 10^{-4}$ grams cm$^{-2}$, where $g(\rho_d d)$ is considered most reliably determined. However, for values of $\rho_d = 1$–$7$ g cm$^{-3}$, the particle diameters resulting from $g(\rho_d d)$ are one or two orders of magnitude larger than those deduced by Remy-Battiau. This discrepancy is not considered significant, however, since sample calculations by Remy-Battiau for a lower limit of $10^{-5}$ cm show that only slight changes result in her calculated light intensities and polarizations. Also, as she has noted, the limited number of available observational data and the not completely satisfactory agreement between her calculations and the observations preclude a more accurate determination than the one given.

The study by Öpik of the forward spike of Comet Arend-Roland included the determination of a function $g(d)$ from the observed variation of the brightness along the spike. Assuming the form of equation (25), a value of $k = 3.35$ was found, which is again qualitatively similar to the $g(\rho_d d)$ of Figure 12. The justification for an accurate determination of a size distribution from the brightness variation is open to question, however, in light of the above criticism of the study concerning the time of emission of the forward spike. One direct result of the much later emission times used by Öpik is that the particles which he found to make up the spike were also of a much smaller size $(1 - \mu \sim 1)$ than those we have found to make up either the spike or the normal tail of Comet Arend-Roland.

The determination of such a function $g(d)$ has also been made for the interplanetary dust particles which are responsible for the zodiacal light and the solar F corona. These particles are thought to be of similar size and composition to those in comet dust tails, and Whipple (1955) has even suggested that they may be of cometary origin. One important difference in these studies, though, is that particles for which $1 - \mu > 1$ would not be expected to be present in the interplanetary dust cloud, since they would be blown out of the solar system in relatively short times. Thus a minimum particle size is imposed on the size-distribution function.

Assuming the form of equation (25), the exponent $k$ has been determined for the interplanetary dust particles by comparison with observed surface-density distributions and polarizations of the zodiacal light. Giese (1963) and Elsässer (1963) have obtained good agreement for $k = 2.5$, and Ingham (1963) found $k = 4$. The differences in these results can be traced to different assumptions regarding the light scattering and the spatial variation of the dust-particle density.

Size-distribution functions of the form of equation (25) have also been used in connection with meteoric particles. Of course, it should be noted that these particles have $d \geq 10^{-2}$ cm, which is much larger than comet dust particles. From observations of visual meteors, Watson (1937) has found $k = 5$, and from radio-echo studies, Kaiser (1954) obtained $k = 4$.

Considering that these studies assumed the form of equation (25) with a constant value of $k$, the function $g(\rho_d d)$ of Figure 12 would certainly appear to be a reasonable one. We would emphasize again that our results should be considered well determined only in the range $4 \times 10^{-4} \leq \rho_d d \leq 40 \times 10^{-4}$ grams cm$^{-2}$.

It should also be noted that the optically most important dust-particle diameters quoted above are seen to be consistent with the many previous estimates of $d \sim 1\ \mu$.

© American Astronomical Society • Provided by the NASA Astrophysics Data System

Most significant is the comparison with the results of Liller (1960), which are based purely on a study of the character of the light scattered by the dust particles in the tail of Comet Arend-Roland. He concluded that the particles were probably composed of iron (for which $\rho_d \approx 7$ g cm$^{-3}$) and had a mean diameter of 0.6 $\mu$, while the optically most important diameter quoted above for $\rho_d = 7$ g cm$^{-3}$ is 0.8 $\mu$.

The level of the rates of dust production rates given above may be compared with the estimates of Liller (1960) for Comet Arend-Roland. Since Liller observed the tail during the period considered above, and since the most typical emission time for the particles comprising the tail on these dates corresponded roughly to perihelion, Liller's rates may be most appropriately compared with our values at the time of perihelion. It should also be pointed out that in Liller's estimates the repulsive force on the dust particles was taken to be some 6–7 times that which he calculated for the radiation pressure. This was done to account for other forces, suspected at that time, and since one of the primary conclusions of the present study is that such forces do not exist, a more appropriate comparison is achieved if this factor is removed from his findings. Accordingly, Liller's values become

$$\dot{N}_d \sim 1.5 \times 10^{19} \text{ particles sec}^{-1}\,, \qquad \dot{m}_d \sim 1.2 \times 10^{7} \text{ g sec}^{-1}\,. \tag{26}$$

From equation (20) with $(\dot{N}_d)_{\text{rel}} = 0.6$ and $\rho_d = 7$ g cm$^{-3}$, this value of $\dot{N}_d$ is obtained if $A\phi(\alpha) = 0.08$, the most reasonable of the three values considered above. With this value of $A\phi(\alpha)$, the value of $\dot{m}_d$ at perihelion given previously was

$$\dot{m}_d \approx 7.5 \times 10^{7} \text{ g sec}^{-1}\,, \tag{27}$$

some 6 times as high as Liller's estimate. This difference is ascribable mainly to the manner in which the particle masses are determined—the average particle mass for the size-distribution function $g(\rho_d d)$ is about 3 times the mass which would be obtained from the use of the optically most important diameter.

There is apparently no available information with which the time variation of $\dot{N}_d(t)$ may be compared, although some brief comments will be made in the next section on this matter in connection with a general suggested property of dust comets. Nor are there any observations of the outburst which is held to have occurred on April 2, 1957. Such outbursts have, of course, been observed on many occasions in other comets. This is not surprising, however, since Comet Arend-Roland was not at all well observed on April 2 or on the immediately preceding dates. Also, since the emission rates changed by only a factor of 3 or 4 at the outburst, the brightness should not have increased by more than one or two magnitudes, a change which would probably not have been detectable without detailed observation.

As with the dust production rates, there is not a large body of information with which our gas production rates may be compared. We would point out that the mass flow rate of the head gas given in Table 4 at perihelion for $A\phi(\alpha) = 0.08$, $\dot{m}_g = 6 \times 10^{7}$ g sec$^{-1}$, corresponds to $\approx 1.5 \times 10^{30}$ molecules sec$^{-1}$ for a molecular weight of 25. This compares well with the estimate of $10^{30}$–$10^{31}$ molecules sec$^{-1}$ by Biermann and Trefftz (1964), an estimate which includes the invisible components of the head gas and one which was deduced from considerations entirely different from those of this paper. The fact that this relatively high estimate of the head-gas production rate is confirmed may be considered one of the most significant results of the present study.

## VI. A SUGGESTED PROPERTY OF DUST COMETS

Before summarizing our conclusions, we shall cite the results of some additional calculations which tend to further verify the validity of the model and which suggest an

© American Astronomical Society • Provided by the NASA Astrophysics Data System

interesting property of dust comets. The detailed density distributions presented above for Comet Arend-Roland cover the relatively short period of 5 days in the time of observation. While the observed tail angles in the comet orbit plane in this period ($\sim$50°–60° from the radial direction) were well explained, the only bases for an explanation of the tail orientation of this comet at other times were the qualitative considerations given in Paper I in connection with the variation in appearance of the syndyne curves for fixed $1 - \mu$ on different dates of observation.

One possible difficulty in explaining the observed tail orientation of this comet on other dates is obvious: the relatively large amount of dust material emitted before perihelion (including the outburst) will be located at increasing angles to the radial direction on subsequent dates, so that calculated tail orientations would then be much too large. Some rather brief calculations have been performed for Comet Arend-Roland on June 5, 1957 ($t \approx +5.0 \times 10^6$ sec), about a month after the dates considered in the detailed calculations presented above. Surface densities were calculated, based on the above functional parameters, except that $\dot{N}_d(t)$ and $v_i(1 - \mu, t)$ had to be extended to later times. The time function of $v_i(1 - \mu, t)$ was taken to be 0.275 km sec$^{-1}$ for $t > 1.1 \times 10^6$ sec, a direct extrapolation of Figure 4, *b*. If $(\dot{N}_d)_{\rm rel}$ was taken as 0.10 for all $t > 0.75 \times 10^6$ sec, the tail angle in the comet orbit plane was found to be $\epsilon \approx 15°$ on June 5. If $(\dot{N}_d)_{\rm rel}$ was taken to be 0.05 for $t > 1.5 \times 10^6$ sec, a tail angle of $\epsilon \approx 20°$ was obtained. No significant traces of the outburst of emission could be detected—the early emission had effectively been blown out of the tail by June 5. These values for the tail angle $\epsilon$ compare quite favorably with the observed angles of 10°–30° (Brandt and Belton 1966; see also Fig. 2, Paper I), and there would appear to be no difficulty in explaining the tail orientation of Comet Arend-Roland at times other than those originally considered above.

We have also considered the tail-angle orientation for Comet Van Gent 1941d, which has a rather different time behavior from that of Comet Arend-Roland (see Fig. 3, Paper I). The larger tail angles ($\epsilon \sim 90°$) for this comet may be explained by dust emissions concentrated even more strongly at early times than was the case for Comet Arend-Roland, and the fact that the tail angle decreases little, if any, after perihelion requires that there be almost no emission after perihelion. The orientations of the synchrones for emission dates between January 1 and July 1, 1941 (perihelion was on September 3, 1941), are all within 20° of the observed tail orientations during the entire period of observation (July 28–December 13, 1941). Sample calculations were performed for the tail angle on two selected dates, August 1 and November 1, 1941, assuming that the dust emission occurred uniformly during the period January 1–July 1, with no emission at other times. It was found that the observed tail orientations on these dates could easily be explained, and no difficulty would be expected for other dates of observation. In particular, on August 1 the observed tail orientation corresponds to emission in the period January 1–April 1, and the particles emitted on later dates have not yet had time to be swept into the tail. On November 1 the particles emitted between May 1 and July 1 give the proper orientation, and the particles emitted earlier have effectively been blown out of the tail.

The dust emission rate presented above for Comet Arend-Roland is seen to be somewhat higher for times before perihelion than after perihelion. We have just suggested that the dust emission of Comet Van Gent occurred almost entirely before the perihelion passage. This may be compared with the fact that comets with a strong dust component are generally new comets, i.e., those approaching the Sun for the first time (Oort and Schmidt 1951). Since this implies that comets emit more dust during their first perihelion passage than in succeeding ones, we would suggest as a logical extension that new comets generally emit more dust material during their approach to the Sun than during their recession from the Sun.

© American Astronomical Society • Provided by the NASA Astrophysics Data System

## VII. CONCLUSIONS

We may summarize the major results of the present study for dust comets in the following conclusions.

1. The comet nucleus serves as the source of the particles which go to form the dust tail. Dust particles having a wide distribution of particle sizes are released in an essentially continuous manner in time during the period of distinctive cometary phenomena.
2. The dust particles are accelerated outward from the nucleus by drag forces due to the expanding gas in the comet head. This interaction occurs only in a small inner head region, where the gas densities are high and where the gas may be described as a continuum. The terminal velocity imparted to the dust particles in this inner head region is mainly a function of the gas production rate, the dust production rate, and the dust-particle size.
3. After departure from the inner head region, the only significant forces acting on the dust particles are solar gravity and pressure of solar radiation. The latter force repels the dust particles into the dust tail.
4. A hypersonic approximation may be made for the motion of the particles in comet tails. With this approximation, relatively simple expressions for the surface density in comet dust tails may be derived.
5. Observed non-radial dust-tail orientations and the variation of the tail angle with time are explainable by the model described.
6. By comparing calculated surface-density distributions with observed light-intensity distributions, the distribution of dust-particle sizes (essentially constant with time), the dust emission rate as a function of time, the head-gas emission rate as a function of time, and the emission velocities from the inner head region as a function of particle size and time may be determined.
7. For Comet Arend-Roland, dust-particle diameters of the order of 1 $\mu$ are found, consistent with previous estimates. Particle-size distributions are found which are qualitatively similar to those found in studies of the interplanetary dust particles which give rise to the zodiacal light and to one suggested by Remy-Battiau (1964) from an analysis of the continuous spectra from the heads of Comets Arend-Roland and Mrkos.
8. The emission rate of dust for Comet Arend-Roland in the neighborhood of perihelion is found to be $\sim 7.5 \times 10^7$ g sec$^{-1}$, a value similar to a previous estimate of Liller (1960).
9. The gas flow rates for Comet Arend-Roland in the neighborhood of perihelion, $\sim 1.5 \times 10^{30}$ molecules sec$^{-1}$, are found to confirm the relatively high estimates of Biermann and Trefftz (1964).
10. An outburst of dust emission is deduced to have occurred in Comet Arend-Roland on April 2, 1957, about 6 days before the comet's perihelion.
11. The forward spike of Comet Arend-Roland was made up of particles emitted between February 6 and March 1, 1957.
12. A general property of dust-rich comets may be that they emit larger amounts of dust in their approach to the Sun than they do during recession.

This work has been sponsored by the Advanced Research Projects Agency (Ballistic Missile Defense Office) and technically administered by the Fluid Dynamics Branch of the Office of Naval Research under contract Nonr-1841(93).

## REFERENCES

Biermann, L., and Trefftz, E. 1964, *Zs. f. Ap.*, **59**, 1.
Brandt, J. C., and Belton, M. J. S. 1966, *Ap. J. Suppl.*, **13**, 125.
Ceplecha, Z. 1958, *Pub. Czech. Astr. Inst.*, **34**, 13.
Elsässer, H. 1963, *Planet. and Space Sci.*, **11**, 1015.

Finson, M. L., and Probstein, R. F. 1967, Fluid Mech. Lab. Rept. No. 67-4, Mech. Eng. Dept., Massachusetts Institute of Technology.
———. 1968, *Ap. J.*, **154**, 327 (Paper I).
Giese, R. H. 1963, *Space Sci. Rev.*, **1**, 589.
Ingham, M. F. 1963, *Space Sci. Rev.*, **1**, 576.
Kaiser, T. R. 1954, *M.N.*, **114**, 52.
Liller, W. 1960, *Ap. J.*, **132**, 867.
Öpik, E. J. 1958, *Irish A.J.*, **5**, 37.
Oort, J. H., and Schmidt, M. 1951, *B.A.N.*, **11**, 259.
Probstein, R. F. 1968, in *Collection Dedicated to the Sixtieth Birthday of Academician L. I. Sedov*, ed. M. A. Lavrent'ev (Moscow: Izdatel'stvo Akademii Nauk S.S.S.R.) (English ed.: *Problems of Hydrodynamics and Continuum Mechanics* [Philadelphia: Society for Industrial and Applied Mathematics]).
Remy-Battiau, L. 1964, *Bull. cl. sci. Acad. roy Belg.*, 5ème sér., **50**, 74.
Richter, N. 1959, *Monatsber. Deut. Akad. Wiss. Berlin*, **1**, 727.
Růžičková, B., and Plavec, M. 1958, *Pub. Czech. Astr. Inst*, **34**, 35.
Watson, F. 1937, *Harvard Ann.*, **105**, 623.
Whipple, F. L. 1955, *Ap. J.*, **121**, 750.
Wurm, K. 1963, in *The Moon, Meteorites, and Comets*, ed. B. M. Middlehurst and G. P. Kuiper (Chicago: University of Chicago Press), p. 573.

Copyright 1968. The University of Chicago. Printed in U.S A.